Proceedings of ASME Turbo Expo 2022
Turbomachinery Technical Conference and Exposition
GT2022
June 13-17, 2022, Rotterdam, The Netherlands

GT2022-82683

NUMERICAL STUDY OF METHANE PYROLYSIS INSIDE A SINGLE-CHANNEL SHOCK WAVE REFORMER

S. V. Mahmoodi-Jezeh[1], Stefan Tüchler[2], Ghislain Madiot[1], Mark Davidson[3], Pejman Akbari[4], and Colin D. Copeland[1]
1. School of Sustainable Energy Engineering, Simon Fraser University,Surrey, BC V3T 4B7, Canada
2. Department of Mechanical Engineering, University of Bath, Claverton Down, Bath, Somerset BA2 7AY, United Kingdom
3. New Wave Hydrogen, Inc., Gainesville, Florida, USA
4. Department of Mechanical Engineering, California State Polytechnic University, Pomona, CA 91768-4062, USA

ABSTRACT

The paper describes a numerical investigation of the thermal decomposition of methane to hydrogen and carbon within a single-channel, four-port wave rotor using a three-dimensional (3-D), Reynolds-averaged Navier–Stokes (RANS) CFD model. This work is in support of the New Wave Hydrogen, Inc. (NWH_2) proprietary technology development. A Menter's $k-\omega$ SST turbulence is used for the closure of the mean momentum equations and is coupled to multispecies transport equations with a one-step finite-rate chemistry model. The kinetic model is validated based on a set of measurement data of a double-diaphragm shock tube case. To further examine the predictive accuracy of the numerical approach, the results of the 3-D single-channel wave rotor are compared with those of quasi-one-dimensional unsteady model that has been previously reported extensively in literature. It is observed that when the wave rotor channel is exposed to the high-pressure driven gas (HP_{DRVN}) port, a secondary right-running shock wave is generated, which greatly energizes the flow around the HP_{DRVN} port, resulting in large magnitudes of pressure and temperature; and consequently, the cracking of methane into hydrogen and carbon. The comparison between 1-D and 3-D simulation results indicate that the LP_{DRVN} gas penetration is around 75% of the channel width in the case of 1-D, but is below 50% in the 3-D case. Furthermore, the conversion rate of methane in the 3-D case is one order of magnitude smaller than that in the 1-D case.

Key words: wave rotor, turbulence simulation, methane pyrolysis, hydrogen production

1 INTRODUCTION

A wave rotor is a dynamic pressure exchange device that utilizes unsteady shock and expansion waves within the channel to efficiently exchange energy between the fluids that have different energy levels. Wave rotor technology is observed in numerous engineering applications such as a topping component for gas turbines [1], superchargers for IC engines [2], refrigeration cycles [3], and pressure gain combustion systems [4]. These practical applications lead to the motivation of this research, which aims to expound the influence of three-dimensional shock and expansion waves on methane (CH_4) pyrolysis inside a NWH_2 Inc. proprietary, single-channel shock wave reformer. This application of wave rotor technology is a new and exciting use that, if successful could provide a novel method for clean hydrogen production.

1.1 BACKGROUND

Steam methane reforming (SMR) is a conventional methods that are routinely used to produce hydrogen from fossil fuels (e.g., coal, oil, and biomass). Extensive field measurements, laboratory experiments and numerical simulations were conducted to study the performance of SMR [5–8]. In this approach, methane and steam are heated until they react to yield hydrogen (H_2) and carbon dioxide (CO_2). Therefore, this method not only continuously produces greenhouse gases in large quantities, but

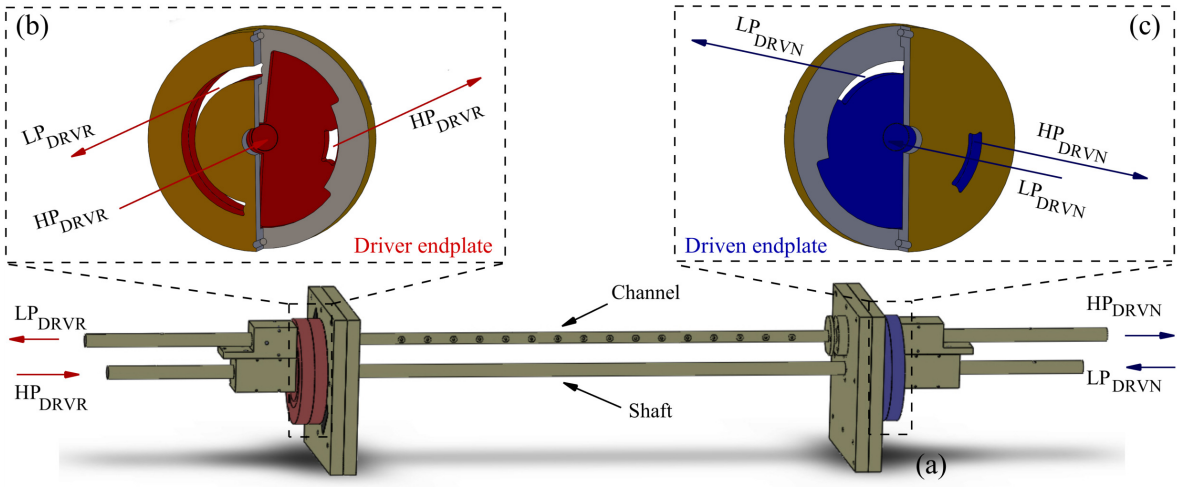

FIGURE 1: (a) A general overview of the design of the NWH_2 single-channel wave reformer with rotating end plates and channel. (b) and (c) A cut-away of driver and driven end plates, respectively. HP and LP refer to high- and low-pressure, respectively. Driver and driven gases are indicated by red and blue colors, respectively.

it also requires a large input of thermal energy which is typically derived from hydrocarbon fuels, further contributing to emission problems. Additionally, the process has a water demand in the production of steam which limits this technology in places that face water limitations and adds a potential water supply impact. Considering the drawbacks of SMR, the direct decomposition of methane from natural gas provides a more environmentally friendly and efficient process. In this process, referred to as methane pyrolysis, methane is heated to temperatures sufficient to break the hydrocarbon bonds and decomposing methane into constituents hydrogen and solid carbon [9, 10]. To efficiently achieve high temperatures required for direct thermal methane decomposition, NWH_2 Inc. has designed and is demonstrating a wave reformer utilizing shock heating [11]. In comparison with SMR, NWH_2 Inc. offers a proprietary high-temperature thermal reforming process that uses no water and produces no direct CO_2 emissions since the solid carbon byproduct is easily captured. The core component is an existing, proven technology (a wave rotor) combined with a well-known process (methane pyrolysis), to produce hydrogen in a low-cost, efficient reactor. The invention overcomes many disadvantages of the existing techniques by employing unsteady shock waves that can produce high temperatures very rapidly with lower energy consumption per unit mass of product. Indeed, the wave reformer benefits from the use of the pressure already embodied in a pipeline or feedstock line and the energy transfer by the shock wave. This is an interesting distinction relative to competing methods of methane pyrolysis.

1.2 DEMONSTRATION DESIGN SYSTEM PRINCIPLE

From a practical point of view, two configurations of wave rotor can be designed: either the drum (housing the shock wave passage(s)) rotates and the end plates remain stationary or the end plates rotate and the drum is stationary. Both approaches have advantages and disadvantageous. For example, the former configuration involves only one moving component (i.e. rotor), but the channel flow is influenced by centrifugal forces brought on by the rotation of the channel. In the latter configuration, there are two moving components, but the stationary shock wave channel makes measurements easier and enables optical access if needed. This approach therefore avoids the difficulties of instrumenting rotating channels. It is also helpful to note that the relative motion is the same for both configurations. Taking advantage of both configurations, the design, build and demonstration of a four-port wave rotor can thus be carried in two phases. The first phase of the experimental demonstration is performed by building and testing a stationary, single-channel with rotating end plates. Understanding of the internal process is fundamental for the investigation and design of any proposed wave rotor. Single-channel experiments can demonstrate the operation of the full multi-channel wave rotor, but with a less complicated system and greater access. The first demonstration test will therefore consist of a single channel and two rotating plates connected to a shaft driven by an electric motor. The design and experimental plan include carefully constructed port aerodynamics and sealing designs. A demonstration of methane pyrolysis (i.e. hydrocarbon thermal decomposition) will be the key outcome in this phase. The success and results of the experiment will be used to design a multi-channel wave rotor in the second phase of the project. Both phases will employ CFD models to support the design and to investigate gas dynamic phenomena occurring in the channels. The present paper will show the single-channel design and CFD analysis with future work detailing the experimental results.

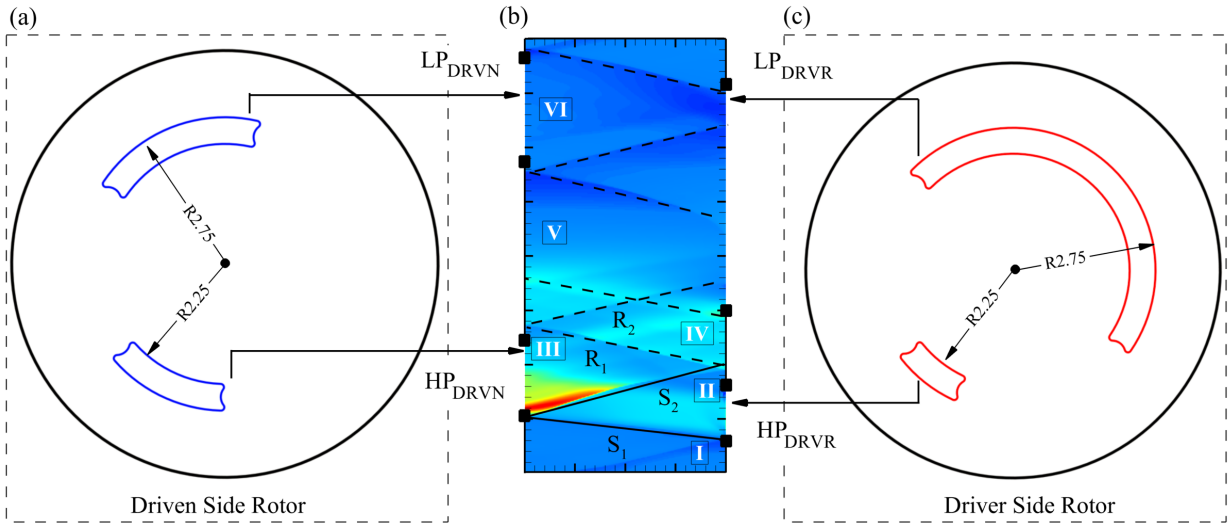

FIGURE 2: Pressure contours and associated wave pattern in the x-t-plane (b) together with the driven and driver end plates ((a) and (c), respectively). Solid black lines denote the expected location of shock waves, while dashed lines represent the head and tail of rarefaction waves.

1.3 SINGLE-CHANNEL WAVE REFORMER DEMONSTRATION SYSTEM

The notion of a device with stationary channels and rotating ports is not new. The concept was initially introduced by Darrieus in 1950 [12]. Since then, several wave rotor studies have adopted the stationary-channel approach to simulate flow fields in both non-reacting [13, 14] and reacting axial wave rotor experiments [15, 16]. Such efforts independently have built and tested simple stationary single-channel configurations using rotary disk valves connected to a shaft driven by an electric motor. To the best of our knowledge, no multi-channel wave devices with stationary channels have been reported in the literature.

Figure1(a) shows a drawing of the single-channel test system that will be analyzed in this paper. The driver gas ports are denoted as CO_2 (shown in red) ports, while driven gas ports are designated as CH_4 (shown in blue) ports. The driver gas and the driven gas enter and exit the channel on the same respective side. Both driver and driven gases enter the end plates through the intake pipes connected to the center of rotating endcaps. The inlet gases fill up the entire volume of the end plates and is released into the channel through the inlet ports when the ports are aligned with the channel. Both compressed driven gas and the expanded driver gas are discharged through the exhaust ports when the ports are aligned with the channel. This process is cyclic and occurs once per revolution of the end plates. Figures1(b) and (c) show a cut-away of driver and driven endplates, respectively. In order to conduct the CFD simulation, the fluid volume and region is extracted from the CAD model of the single-channel device and then meshed using Ansys ICEM. The test cases and numerical method will be detailed in Sec. 3.

Figure 2 shows a schematic of a front view of the driven and driver side rotors (Figs. (a) and (c), respectively) and shows an example of the pressure field and the spatial distribution of shock and expansion waves for a single-channel wave reformer ((Fig. (b)). The example shown here is a reverse-flow design with two inlet (LP_{DRVN} and HP_{DRVR}) and two outlet ports (HP_{DRVN} and LP_{DRVR}). The single-channel wave reformer has three high- (i.e., II, III and IV) and low-pressure regions (i.e., I, V and VI) inside the rotor.

It should be understood that the top of each wave diagram is looped around and joined to the bottom of the diagram, that is, each wave cycle is repetitive. In Fig. 2, the low-pressure driven (LP_{DRVN}) gas enters the wave rotor at low pressure and temperature through the LP_{DRVN} port at section VI. As the rotor rotates, the rotor channels, partially filled with the driven gas are exposed to the high-pressure driver (HP_{DRVR}) gas port when they are aligned with that port. Due to the pressure difference between the driver and driven gases, the driver gas is forced into the channels. This also initiates primary and reflected shock waves (marked with 'S_1' and 'S_2', respectively) that pass through the channels and compresses the driven fluid within the channels at section II. The driver gas properties determine the shock strengths generated within the device. Continuous rotation of the closed end plates brings the channel flow to rest. The energized driven fluid leaves the channels through the corresponding outlet port by expansion waves (marked with 'R_1') generated at the channel ends at section III. By further rotation, the deenergized driver gas is also scavenged out of the passage through the corresponding outlet port and the cycle repeats itself at section V. By carefully selecting port locations and their widths,

an efficient transfer of energy can be obtained between flows in the connected ducts with only minor mixing effects at the gas interfaces.

1.4 LITERATURE SURVEY

In the early 1950s, Glick [17] extended the application of unsteady waves to heat a gas to high reaction temperatures to promote the formation of useful products through the pyrolysis of various hydrocarbon fuels. Glick *et al*. [18] also conducted a series of investigations into the thermal fixation of nitrogen directly from air by the generation of nitrogen oxide (*NO*) by the proper heating and subsequent rapid cooling of air in a chemical shock tube. Rose [19] reported *NO* production in concentrations of 5-7% at high temperatures and pressures (approximately 3000 *K* and 100 *atm*), sufficient for economic recovery. Their studies led to a successful series of experiments which provided data on the kinetic rates of *NO* formation and demonstrated conclusively that nitrogen could be fixed by means of a combination of shock waves and expansion waves in controlled temperature pulses.

In laboratory work, Wilson *et al*. [20] performed measurements in a four-port through-flow wave rotor using tube-type combination pressure probes, and concluded that the performance of the wave rotor is mainly characterised by the temperature ratio across the wave rotor, loop flow ratio, inlet mass flow rate, rotor speed, and also leakage paths. This is evidenced by the studies of Brouillette [21] and Iancu *et al*. [22] who investigated shock wave compression in a microchannel using experimental and numerical approaches, respectively. To study the effect of finite tube opening time and leakage from the tube on the unsteady flows within the rotor passage, Welch *et al*. [23] developed a one-dimensional computational code to calculate the wave rotor pressure gain and burner loop pressure drop for specified turbine inlet temperature. Araki *et al*. [14] measured the turbulent flow inside a microwave rotor cell using laser-Doppler velocimeter (LDV). In their experiment, the pressure ratio and rotor speed of the wave rotor was set at 2.5 and 5,000 rpm, respectively. They observed that the magnitude of velocity within the channel increases and decreases rapidly due to the existence of shock waves. Okamoto and Nagashima [13] investigated the wave rotor inner flow dynamics experimentally and numerically. They showed that the primary and secondary shock waves are highly sensitive to the gradual passage opening and leakage through the clearance, respectively. Kurec [24] conducted particle image velocimetry (PIV) and RANS simulations for studying the unsteady flow inside a stationary passage of a pressure wave exchanger. They demonstrated that $k-\omega$ SST can well predict the major characteristics of the flow such as penetration length high pressure gases into the flow passage. The effect of port arrangement on the performance of wave rotor refrigerator (WRR) was experimentally and numerically investigated by Hu *et al*. [25]. They observed that the performance of the system is strongly influenced by with the geometrical arrangements as the coefficient of performance (COP) of the WRR is apparently decreased by 41.8% with improper port widths or positions. More recently, Tüchler and Copeland [26] conducted detailed experiments to characterize the wave rotor turbine performance through variation of several parameters such as loop flow ratio, axial leakage, and hot inlet gas temperature. In their follow-up study, Tüchler and Copeland [27] optimised four port throughflow micro-wave rotor with non-axial channel shape using experimental testing and a quasi-one-dimensional CFD code. They observed that at a fraction of the rotational speed of comparable turbomachinery, wave rotor shock wave compression is highly efficient and shaft power extraction can be obtained within the non-axial wave rotor channel.

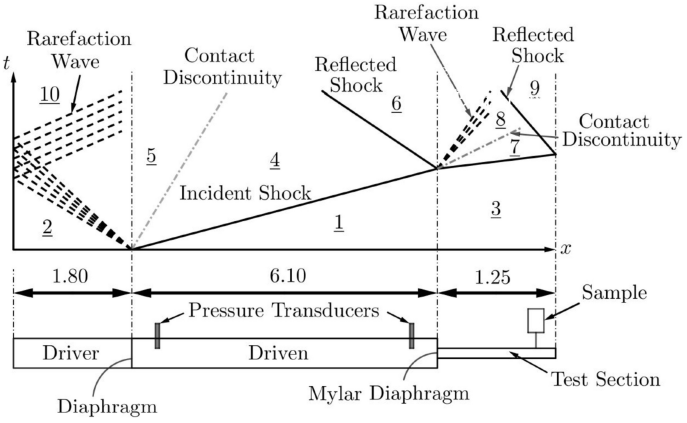

FIGURE 3: Schematic of experimental set-up and definition of the time-space diagram indicating the evolution of the shock-wave, the contact surface, and the expansion fan. The origin of the absolute coordinate system $[x,r]$ is located at the inlet of the driver section of the shock tube. The vertical red dashed lines demarcate diaphragms that separate the shock tube into three different parts (i.e., driver, driven and test sections).

Notwithstanding the aforementioned contributions, a RANS CFD study of 3-D single-channel wave rotor flows is still lacking in the current literature and many questions regarding the fundamentals of the flow physics remain open. Furthermore, no RANS CFD results on the 3-D single-channel wave rotor flows have been published thus far. In doing so, we aim at performing a RANS CFD study of NWH_2 single-channel wave rotor flows to obtain a detailed knowledge of unsteady wave motions through a three-dimensional model of a single-channel wave rotor. Furthermore, the results of this simulation are compared with those from the quasi-1-D model created by Tüchler and Copeland. A thorough description of the numerical method and validations of the quasi-1-D approach can be found in reference [27].

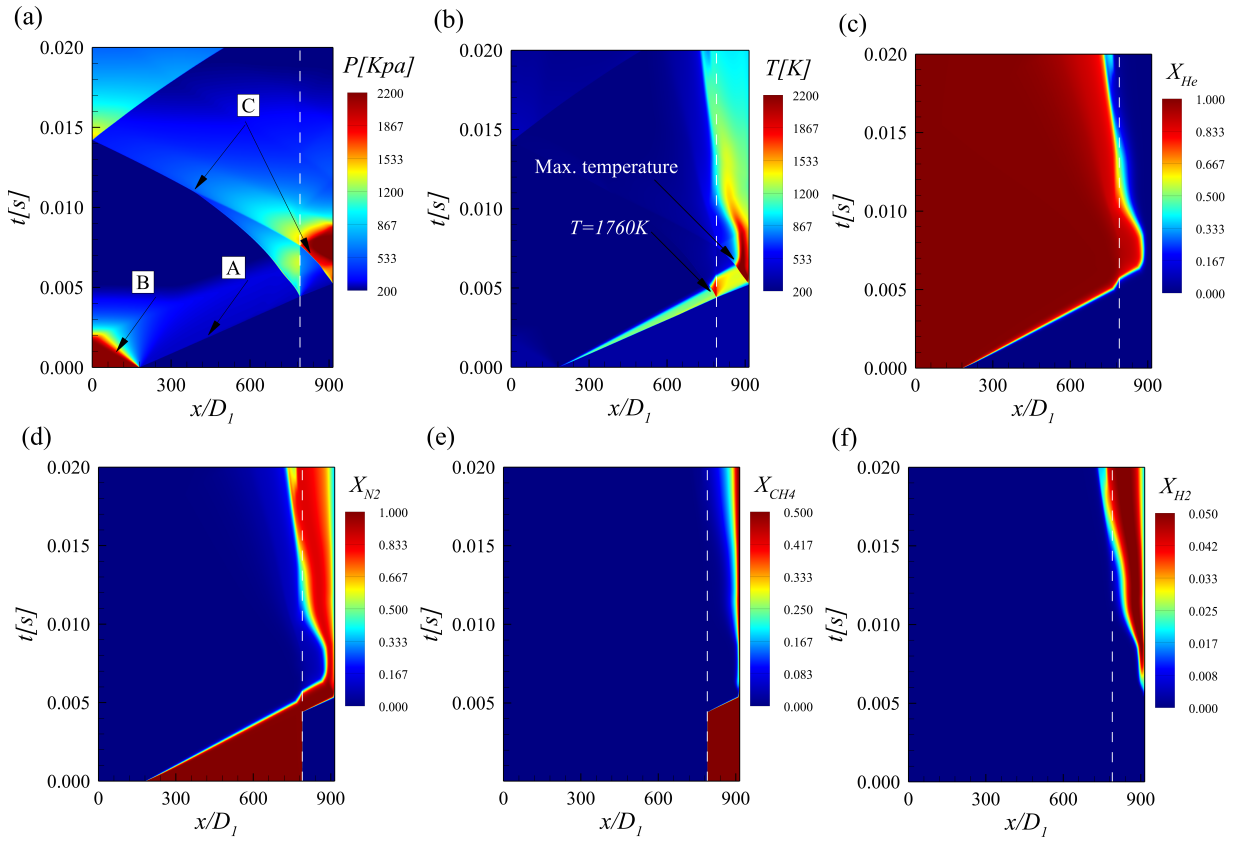

FIGURE 4: Contours of the mean pressure (a), temperature (b), and mole fraction of the helium, nitrogen, methane and hydrogen (c), (d), (e), and (f), respectively in the x-t plane. The vertical white dashed line demarcates the trailing edge of the test section. The axial domin length is non-dimensionalized using the diameter of the driver and driven sections (D_1).

2 SHOCK TUBE EXPERIMENTS - MODEL VALIDATION

It is critical to analyse the wave rotor reformer cycle bearing in mind the influence of chemical reactions on the temperature field, and to validate the turbulence chemistry interaction model with a classical test case of a shock tube. The experiments were conducted at the University of Florida (UF) in a shock tube that has a driver section of 1.8 m and a driven section of 6.1 m. Both sections have a diameter of $D_1 = 0.1\,m$. For the purpose of this work, a test section of 1.25 m with inner diameter of $D_2 = 0.035\,m$ is attached at the end of the driven section. Prior to the experiment starting, this section separated the methane under study from the inert gas in the driven tube by a thin Mylar diaphragm such that it would not affect the strength of the incident shock-wave. Figure 3 shows a schematic of the experimental set-up and the respective states within the shock tube at different locations and instances in time. In this study, the driver section is filled with Helium (He) with the initial pressure 2170 KPa, while the driven and test sections are filled by Nitrogen (N_2) and Methane (CH_4), respectively, with the initial pressure 13.8 KPa. The initial temperature is set at 300 K for all three different sections. The sample collection was separated from the test section by a fast-response solenoid valve. The shock tube was equipped with dynamic pressure transducers with a scan rate of 5 MHz enabling computation of the shock speed of the incident shock wave and thus providing additional validation for the wave dynamics of the numerical model. Experimental control was supported by two-DAQ boards, 5 Mb/s channel and 1.25 Mb/s, respectively.

In order to build confidence in the accuracy the simulations, our RANS CFD results were compared against the reported experimental data from UF. The RANS simulation of the shock tube flow was performed with a axial domain size $L = 915\,D_1$, where D_1 is the diameter of the driver and driven sections. Th shock tube diameter for the test section was set to $D_2 = 0.035\,m$, identical to that used in the UF shock tube. A no-slip and adiabatic conditions were prescribed at all four sidewalls. The number of grid points used in our RANS CFD simulation was 1700×60 along the x and r directions, respectively. The mesh was non-uniform in the wall-normal direction and was refined near the bottom and top solid surfaces.

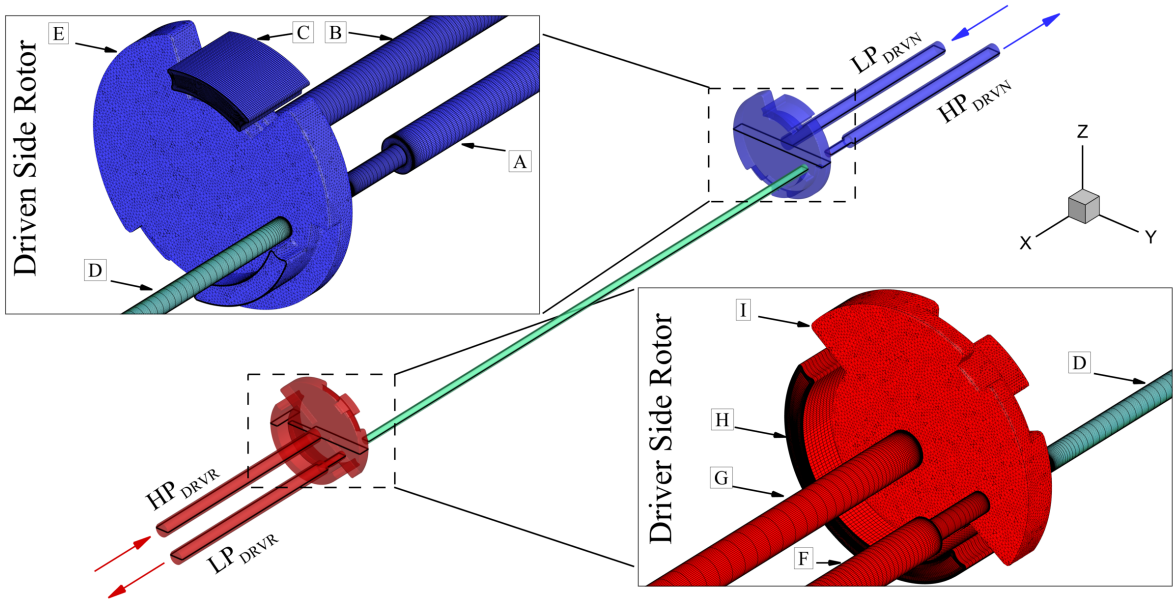

FIGURE 5: Schematic of the 3-D single-channel wave rotor with grid system. The origin of the coordinate system $[x,y,z]$ is located at the centre of the cross section of the channel near the driven side rotor. In order to show clearly the parts of the driven and driver side rotor, they are partially enlarged and replotted. HP and LP refer to high- and low-pressure, respectively.

The method for hydrogen production with sequestration of carbon is the thermal decomposition of methane. When methane is heated to high temperature, the methane decomposes to carbon and hydrogen:

$$CH_4 \longrightarrow C + 2H_2, \quad \Delta H = +75.4 \text{ KJ/mol} \quad . \tag{1}$$

The endothermic energy required to perform this reaction is 75.4 KJ/mol to produce 2 mols of hydrogen and the temperature must be above $973\,K$ for the reaction to proceed at a reasonable rate [9]. The reaction mechanism used in this study employs a simple one-step irreversible reaction, which turns the reactant (methane) into products (hydrogen and carbon). The forward reaction rate for methane cracking is evaluated using a modified Arrhenius equation as follows:

$$K_f = AT^n e^{\frac{-E_a}{RT}} [CH_4]^a \quad . \tag{2}$$

In this equation, A denotes the pr-exponential factor, n is the Arrhenius rate, E_a represents the reaction activation energy, R is the universal gas constant, and T and a denote the local temperature and the reaction order/rate exponent, respectively. In order to determine all parameters of the reaction rate, the ensuing system of equations was solved numerically and the parameters fitted using a least-squares approach to experimental data from the open literature [28]. The parameter fitted for methane pyrolysis used in our RANS simulation is summarized in Table 1.

TABLE 1: Fitted modified Arrhenius parameters for the one-step chemistry model.

Pr-exponential factor $[1/s]$	Arrhenius rate	Activation energy $[J/kgmol]$
6.088×10^6	0.1	1.825×10^8

Figure 4 shows the contours of the mean pressure, temperature, and mole fraction of the helium, nitrogen, methane and hydrogen in the x-t plane. From this figure, it is found that after rupture of the diaphragm at $t = 0$, a right-running incident shock wave (marked with 'A') is triggered by the high-pressure gas within the driver section and increases the temperature of the driven gas as the shock wave travels downstream. At the same time, a rarefaction wave (marked with 'B') expands the Helium within the driver section and is reflected off the left-hand sidewall. Due to the high-pressure ratio, the flow induced by the incident shock wave is supersonic and the driver gas penetrates the driven section. Upon reaching the area contraction, a first reflected shock wave (marked with 'C') is formed that coincides

TABLE 2: Comparison of experimental and numerical results. Percentage values in parentheses indicates relative error between experimental and numerical.

Methods	Methane conversion $X[\%]$	Shock speed $u\,[m/s]$
Experiments	12.8	1184
RANS simulation	13.25 (+3.39%)	1243 (+4.74%)

TABLE 3: Summary of boundary condition for the 3-D single-channel wave rotor case.

	P $[KPa]$	T $[K]$
HP_{DRVR}	4000	950
HP_{DRVN}	2500	1400
LP_{DRVR}	100	900
LP_{DRVN}	266	773

with the location of the peak temperature within the shock tube. Looking at the species contours it becomes apparent that this process provides sufficient shock heating for methane pyrolysis to commence and the subsequent formation of hydrogen. As shown in Fig. 4(b), the value of temperature is around $T = 1760\,K$ close to the trailing edge of the test section, where the reflected shock wave forms (see Fig. 4(a)). This is in very good agreement with $T = 1727\,K$ from the experiments. The estimated values for the conversion rate of methane (i.e., $X = (M/2)/((M/2)+1)$, where M denotes the molar ratio of hydrogen and methane) and shock speed behind the second shock wave in region 6 also exhibit good agreement with the with experimental data, as laid out in Table 2.

3 TEST CASES AND NUMERICAL METHOD

Figure 5 shows the 3-D computational domain of the NWH2 Inc. proprietary single-channel wave rotor and mesh used in our RANS 3-D CFD model. The axial-length of the circular channel is set to $L = 152\,R$, where R is the channel radius. In this study, the driver and driven gases enter the end plates at an inlet temperature $950\,K$ and $773\,K$, respectively, through the central pipes connected to the rotating end caps. The streamwise domain length of the central pipes is $L_x = 25\,R$. This rig operates on a reverse-flow wave cycle where the gas streams enter and leave the channel from the same end. In this study, the simulation is performed based on the constant pressure ratio $PR = P_{HP_{DRVR}}/P_{LP_{DRVN}} = 15$, where $P_{HP_{DRVR}}$ and $P_{LP_{DRVN}}$ denote the inlet pressure of driver and driven gases, respectively. A no-slip condition along with zero normal gradients of species mass fractions and an adiabatic condition are imposed on all solid walls.The single-channel wave rotor rotational speed is maintained at the design speed of 2000 rpm. The boundary conditions and opening and closing timings of the ports are summarized in Tables 3 and 4, respectively.

In order to simulate the 3-D turbulent flow inside the single-channel wave rotor, a transient simulation is carried out using the commercial CFD solver Ansys Fluent R20.1. The governing equations for continuity, momentum, energy, and species transport are solved using the unsteady RANS equations with turbulence closure provided through the $k-\omega$ SST turbulence model. The finite rate model is also employed to account for the turbulence-chemistry interaction. The numerical algorithm is

TABLE 4: Summary of port timings for the single-channel shock wave reformer. Here, θ_{max} is set at 360^o for our 3-D RANS simulation.

Ports	Open (θ/θ_{max})	Close (θ/θ_{max})
HP_{DRVR}	0.078	0.183
HP_{DRVN}	0.147	0.308
LP_{DRVR}	0.383	0.885
LP_{DRVN}	0.747	0.968

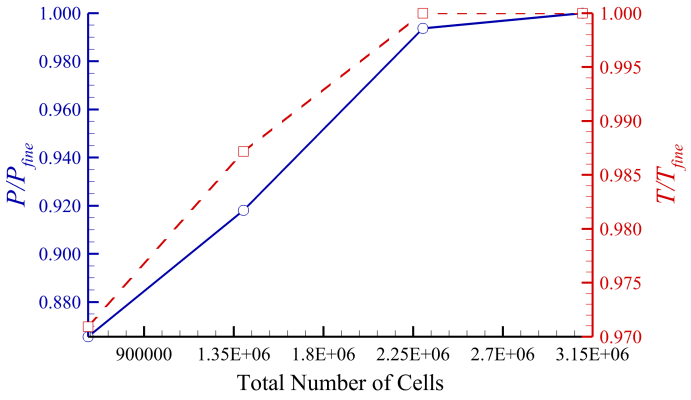

FIGURE 6: Normalised results for both the pressure and temperature near the HP_{DRVN} port at $(x/L, \theta/\theta_{max}) = (0.0, 0.15)$ as a function of cell count. The pressure and temperature terms are non-dimensionalized using the data of the finest grid solution.

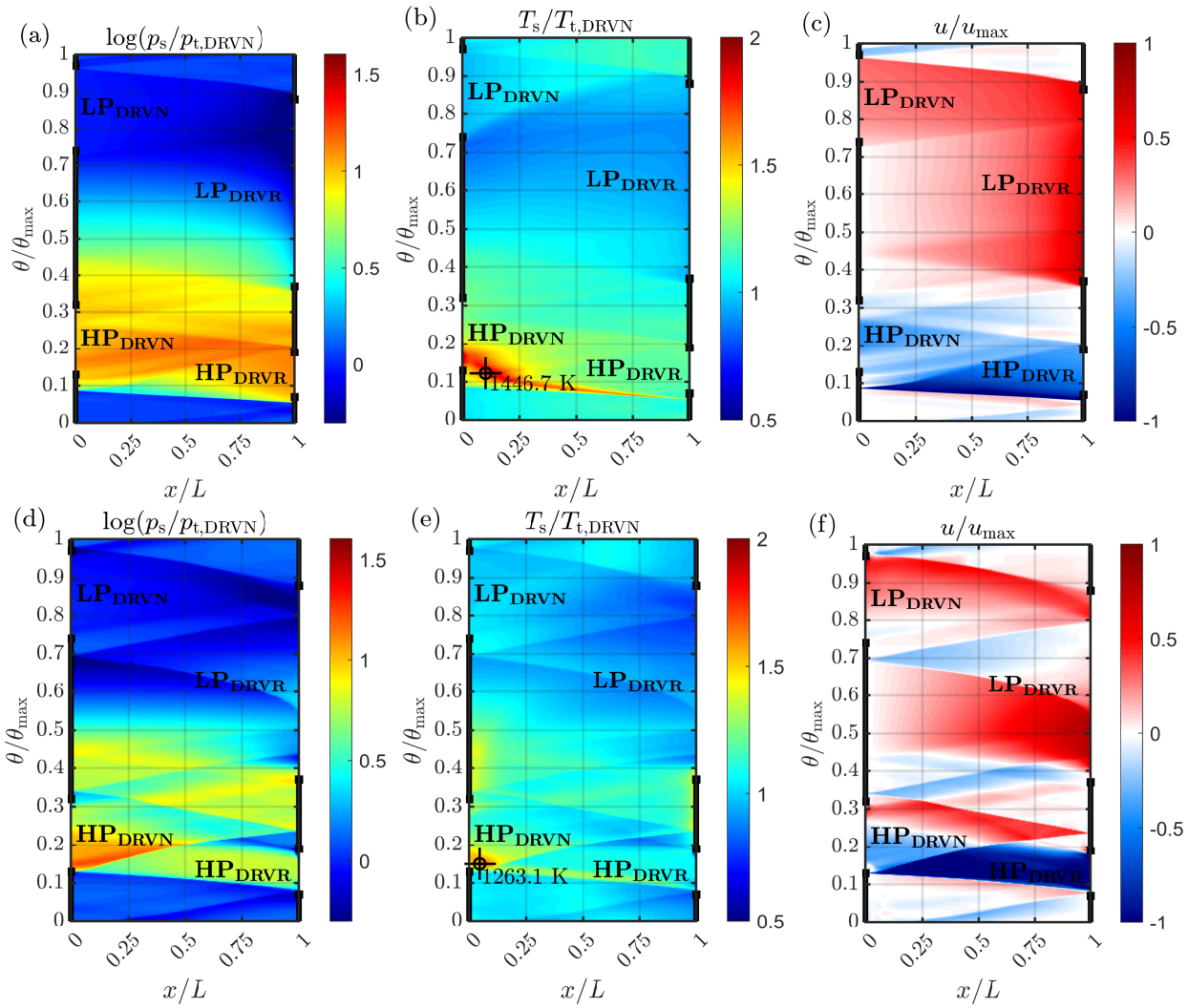

FIGURE 7: Contours of non-dimensionalized mean pressure, temperature and streamwise velocity (P_s, T_s and u) along the central streamwise line located at $(y,z) = (0,0)$ for 1-D (a, b, c) and 3-D (d, e, f) simulations. The z-coordinate indicates to the axial coordinate and follows the length of the channel, while θ denotes the azimuth position of the channel at a certain time t.

based on the finite-volume method in which a second-order accuracy is achieved with respect to both spatial and temporal discretizations. A fractional-step method is applied and a pressure correction equation is solved using the parallel algebraic multigrid solver, and the convergence of the solver is considered once the averaged residue of a discretized algebraic equation drops below 10^{-5}. For time advancement, the Courant–Friedrichs–Lewy (CFL) number is approximately 0.5.

In this study, we used two types of grids to precisely simulate precisely turbulent flow inside the single-channel wave rotor: one multi-block structured (for *HP* and LP_{DRVN} pipes, *HP* and LP_{DRVR} pipes, as well as circular channel) and the other unstructured (for both driver and driven sides of the rotor). The multi-block structured grid (STR-OH) has an O-H configuration (marked with '*A*' , '*B*', '*C*' , '*D*', '*F*' , '*G*', and '*H*'), as shown in Fig. 5 to remove the highly skewed cells for a circular channel. While the unstructured grid (UNSTR) (marked with '*E*' , and '*I*') is fully tetrahedral whereby the cells are allowed to be assembled freely within the computational domain. Both STR-OH and UNSTR grids are designed to have ten points to define the mixing-layer momentum thickness. To carefully evaluate the grid resolutions used for our RANS CFD simulation, four different mesh resolutions were evaluated ranging from approximately 620,000 to 3,100,000 cells. Figure 6 shows the variation of both the pressure and temperature near the HP_{DRVN} port at $(x/L, \theta/\theta_{max}) = (0.0, 0.15)$ as a function of cell count. From this figure, it is seen that the error between the mesh employed for our simulation and the finest solutions for both pressure and

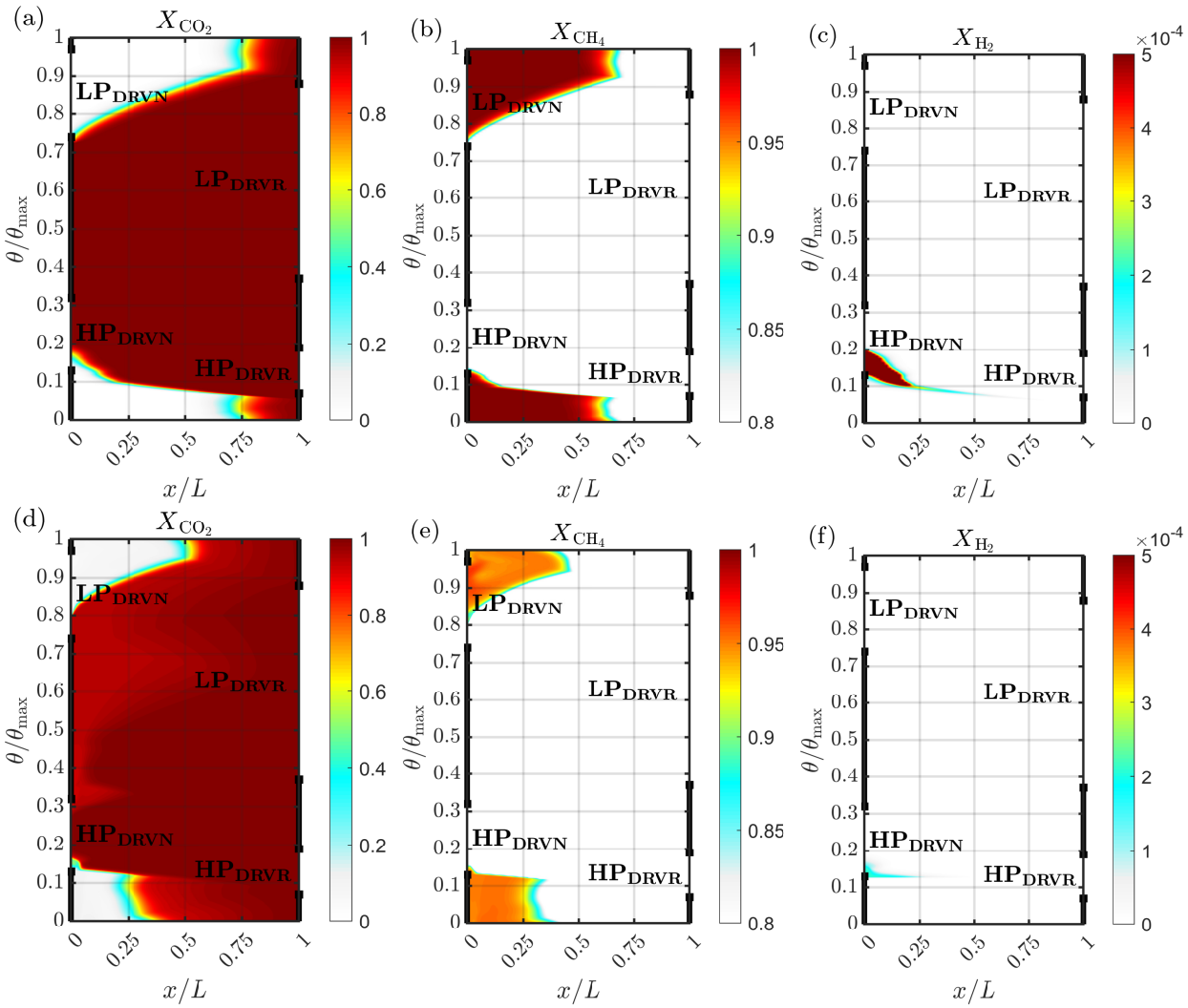

FIGURE 8: Contours of mole fraction of carbon dioxide, methane, and hydrogen (X_{CO_2}, X_{CH_4}, and X_{H_2}, respectively) along the central streamwise line located at $(y,z) = (0,0)$ for 1-D (a, b, c) and 3-D (d, e, f) simulations.

temperature terms is less than 1%, indicating that the grid resolution of the RANS is satisfied in the present study.

4 RESULTS AND DISCUSSION

Figure 7 compares the contours of non-dimensionalized mean pressure, temperature and streamwise velocity (P_s, T_s and u, respectively) along the central streamwise line located at $(y,z) = (0,0)$ for two simulations. By comparing Figs. 7(a) with 7(d), it is apparent that near the HP_{DRVR} port (at $x/L = 1.0$), the magnitude of $\log(P_s/P_{t,DRVN})$ of the 3-D simulation is lower than that of the 1-D simulation, leading to compromise of the strength of the primary shock wave. As a result, a less pressure rise occurs near the HP_{DRVN} port at $x/L = 0.0$ in the 3-D simulation case. This phenomenon is mainly because the turbulent flow inside the HP_{DRVR} pipe intensively interacts with the windward face of the driver rotor, causing the flow to become stagnant and create a high pressure region. This further leads to a reduction in the magnitude of pressure at the entrance of HP_{DRVR} port or a generation of pressure difference between the inlet of HP_{DRVR} pipe and HP_{DRVR} port. The interaction between primary shock wave and HP_{DRVN} port are the underlying physical causes of the generation of a right-running secondary shock wave and the appearance of a local maximum in the contours of mean pressure (see Figs. 7(a) and (d)) and temperature (see Figs. 7(b) and (e)). This explains the unsteady nature of the flow inside the single-channel wave rotor and shows how the primary and secondary shock waves lead to an exchange of energy between the fluids that have different levels of energy. Furthermore, in comparison with the 3-D case, the effects of shock waves on the major char-

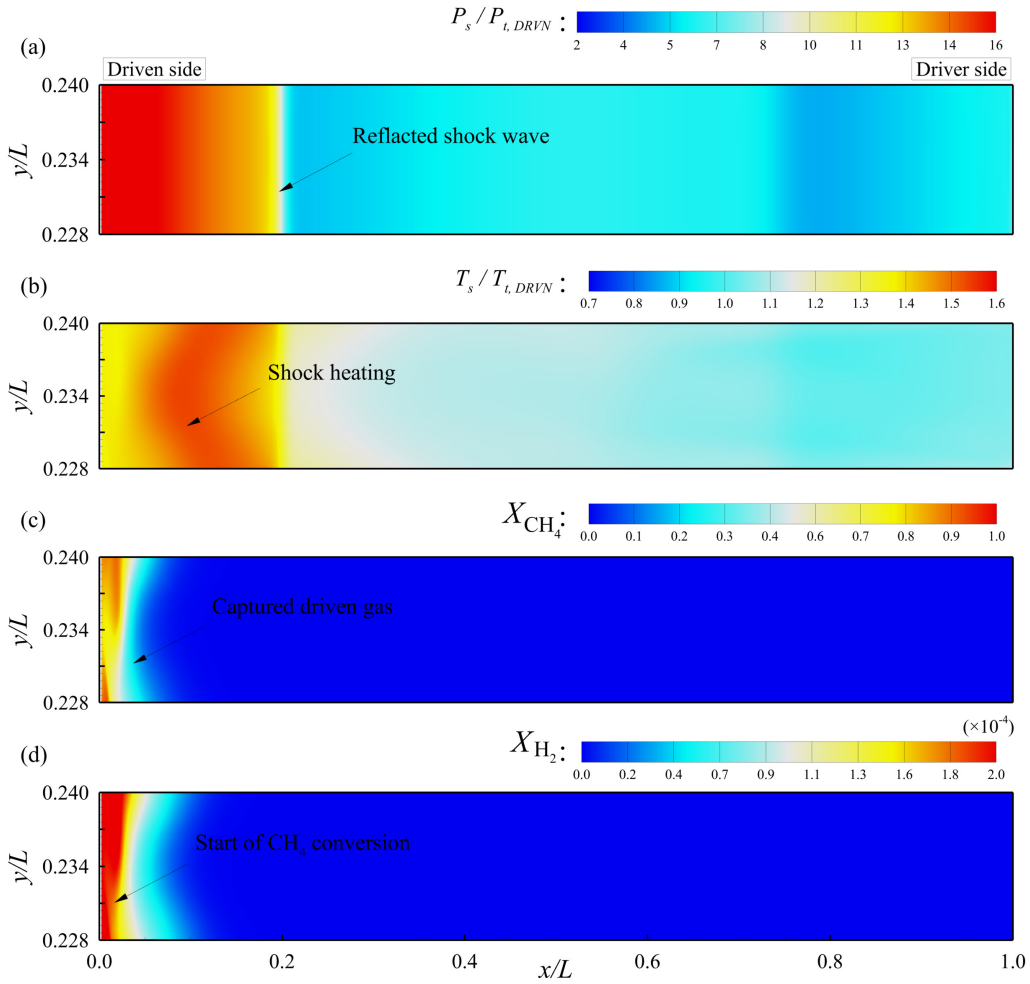

FIGURE 9: Contours of the non-dimensionalized mean pressure (a), temperature (b) and mole fraction of $CH4$ and H_2 ((c) and (d), respectively) in the central x-y plane (at $\theta/\theta_{max} = 0.13$) for the 3-D simulation case.

acteristics of the flow in the 1-D case are less pronounced near the LP_{DRVR} and LP_{DRVN} ports, leading to a more uniform distribution of P_s, T_s and u in these regions. By comparing Figs. 7(c) and (f), it is apparent that in the 3-D simulation case, the value of the mean streamwise velocity transitions from being negative to being positive as the channel is exposed to the end of the HP_{DRVN} port, whereas in the 1-D simulation case, the sign of the mean streamwise velocity remains unchanged over the HP_{DRVN} port.

Figure 8 shows the contours of mole fraction of carbon dioxide, methane, and hydrogen (X_{CO_2}, X_{CH_4}, and X_{H_2}, respectively) along the central streamwise line located at $(y,z) = (0,0)$ for two simulations. From this figure, it is seen that the scavenging and penetration length of driven gas in 1-D case are different from those of the 3-D case since the LP_{DRVN} gas penetration is around 75% of the channel width in the case of 1-D, but is below 50% in the 3-D case. Furthermore, it is it is clear that in the 3-D case, there is a certain amount of driver gases that do not leave the channel through the LP_{DRVR} port, but are carried over through the LP_{DRVN} port. This will further cause the mixing and interaction of driven and driver gases within the driven side rotor for 3-D case. Figures 8 (c) and (f) indicate that in the region near the HP_{DRVN} port, the endothermic heat is provided to the channel by the shock compression, which causes methane cracking; and consequently the generation of the molar concentration of hydrogen. The methane pyrolysis reaction is a highly endothermic process, which absorbs thermal energy from its surroundings. By comparing Figs. 7(a) with 7(d), it is observed that the value of X_{H_2} in 3-D case is one order of magnitude smaller than that in the 1-D case. This is simply because the decaying rates of $\log(P_s/P_{t,DRVN})$ in 3-D case is faster than those of the 1-D case over the HP_{DRVN} port (see Fig. 9(a)) due to the gradual passage opening effects, which consequently leads to less temperature

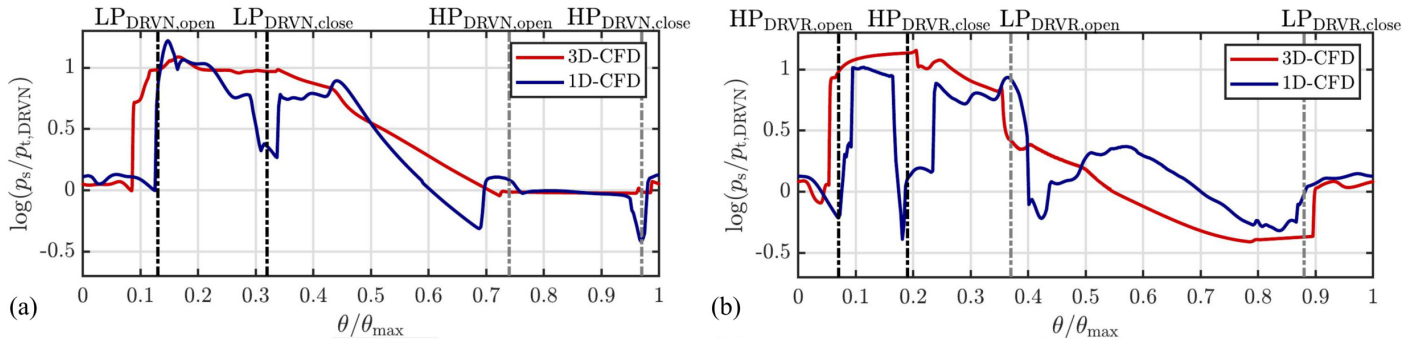

FIGURE 10: Profiles of the non-dimensionalized mean pressure, $\log(P_s/P_{t,DRVN})$, of the two different simulations at the driven (a) and driver (b) side of the rotors.

rise and less generation of H_2 mole.

To better visualize the turbulent flow dynamics inside the channel, the distributions of the non-dimensionalized mean pressure, temperature and mole fraction of CH_4 and H_2 are demonstrated in the central x-y plane (at $\theta/\theta_{max} = 0.13$) in Fig. 9. This figure clearly shows that due to the reflection of the left-running primary shock waves, the magnitudes of both $P_s/P_{t,DRVN}$ and $T_s/T_{t,DRVN}$ increase, and a positive peak occurs in their contours close to the driven side of the rotor (see Figs. 9(a) and (b)). This phenomenon also leads to the compression of the driven gas and the generation of a region denoted as "captured gas" near the left end of the channel (at $x/L = 0.0$). This result is consistent with the large-eddy simulation (LES) result of Hu *et al*. [29] who studied the effects of different operation parameters, such as rational speed and overall pressure ratio on the wave rotor refrigerator performance. Within localized compression zones, the rate of methane conversion increases strongly with temperature and the CH_4 mole starts decomposing into hydrogen.

Figures 10(a) and (b) compare the profiles of the non-dimensionalized mean pressure, $\log(P_s/P_{t,DRVN})$, of the two different simulations at the driven and driver side of the rotors, respectively. From figure 10(a) it is seen that for both simulations, the magnitude of the $\log(P_s/P_{t,DRVN})$ peaks in the neighbourhood HP_{DRVN} port at $\theta/\theta_{max} = 0.14$ (owning to the formation of reflected shock wave) and then decreases as the value of angular position θ/θ_{max} increases. This figure also shows that due to the gradual passage opening effect, the profile of $\log(P_s/P_{t,DRVN})$ in the 3-D simulation case manifests two distinct peaks at $\theta/\theta_{max} = 0.15$ and 0.75 (i.e., when channel is exposed to the HP_{DRVN} and LP_{DRVN} ports, respectively). In the 1-D model, gradual passage opening effects are not modelled and it is assumed the channels are exposed instantly to the port flow. From figure 10(b) it is seen that the wave action in the 3-D simulation case is more pronounced than that of the 1-D case, leading to the stronger expansion on the driven side of the rotor in 3-D case. This phenomenon also causes an increase in the communication between the flow near the driver and driven side of the rotors.

5 CONCLUSION

Reynolds-averaged Navier–Stokes is performed to study the effects of 3-D shock and expansion waves on the methane (CH_4) pyrolysis inside NWH_2 Inc. proprietary single-channel shock wave reformer. In order to carefully evaluate all parameters of the reaction rate used for our 3-D RANS simulation, one additional numerical simulation has been conducted based on the test cases of shock tube and its results are validated against the experimental tests from UF. Furthermore, the results of 3-D single-channel wave rotor are compared with those of a quasi-1-D model one developed by Tüchler and Copeland [26]. Results show that although the contour patterns of pressure and temperature of 1-D simulation are similar to those of the 3-D simulation, they are notable differences. The reason is that in a 1-D simulation, the gradual opening and closing of the rotor passages as well as unsteady characteristics of turbulent separations inside the channel are not modeled and it is assumed the channels are exposed instantly to the port flow, causing non-physical results. This reveals the fact that a full 3-D simulation is necessary for a reliable prediction of the conversion rate of $CH4$ inside a single-channel wave reformer. For example, it is found that the secondary shock wave strength in the 1-D case is higher than that of the 3-D case, which subsequently causes the appearance of the higher temperature and more decomposing leave of driven gas close to the HP_{DRVN} port. This paper provides a useful insight into the process of developing a single channel wave rotor that is able to achieve methane decomposition through shock wave heating. This proprietary technology holds significant promise in the production of hydrogen from methane that also allows solid carbon to be easily separated as a byproduct. Ongoing experimental testing by NWH_2 Inc. that will be reported in future publications based on the designs analyzed in this paper.

ACKNOWLEDGMENT

The authors would like to thank and acknowledge New Wave Hydrogen, Inc. (NWH2) and co-funding groups including,

Emissions Reduction Alberta (ERA), Total Energies, the Natural Gas Innovation Fund (NGIF) and its members, and GRTgaz.

REFERENCES

[1] Akbari, P., Nalim, R., and Müller, N., 2006. "Performance enhancement of microturbine engines topped with wave rotors". *J. Eng. Gas Turbines Power,* ***128***(1), pp. 190–202.

[2] Lei, Y., Zhou, D. S., and Zhang, H. G., 2010. "Investigation on performance of a compression-ignition engine with pressure-wave supercharger". *Energy,* ***35***(1), pp. 85–93.

[3] Zhao, J. Q., Hu, D. P., Liu, P. Q., Liu, F. X., and Gao, J. J., 2013. "Thermodynamic analysis a novel wave rotor refrigeration cycle". *Adv. Mater. Res.,* ***805***, pp. 537–542.

[4] Nalim, M., 1999. "Preliminary assessment of combustion modes for internal combustion wave rotors". *ASME J. Eng. Gas Turbines Power,* ***121***(2), pp. 265–271.

[5] Rosen, M. A., 1991. "Thermodynamic investigation of hydrogen production by steam-methane reforming". *Int. J. Hydrogen Energy,* ***16***(3), pp. 207–217.

[6] Adris, A. M., Pruden, B. B., Lim, C. J., and Grace, J. R., 1996. "On the reported attempts to radically improve the performance of the steam methane reforming reactor". *Can. J. Chem. Eng.,* ***74***(2), pp. 177–186.

[7] Boyano, A., Blanco-Marigorta, A. M., Morosuk, T., and Tsatsaronis, G., 2011. "Exergoenvironmental analysis of a steam methane reforming process for hydrogen production". *Energy,* ***36***(4), pp. 2202–2214.

[8] Tugnoli, A., Landucci, G., and Cozzani, V., 2008. "Sustainability assessment of hydrogen production by steam reforming". *Int. J. Hydrogen Energy,* ***33***(16), pp. 4345–4357.

[9] Steinberg, M., 1998. "Production of hydrogen and methanol from natural gas with reduced CO2 emission". *Int. J. Hydrogen Energy,* ***23***, pp. 419–425.

[10] Dunker, A. M., Kumar, S., and Mulawa, P. A., 2006. "Production of hydrogen by thermal decomposition of methane in a fluidized-bed reactor—effects of catalyst, temperature, and residence time". *Int. J. Hydrogen Energy,* ***31***(4), pp. 473–484.

[11] Akbari, P., Tüchler, S., Copeland, C. D., and Mahmoodi-Jezeh, S. V., 2021. "Shock wave heating: a novel method for low-cost hydrogen production". *2021 International Mechanical Engineering Congress and Exposition. IMECE2021-69775*.

[12] Georges, D., 1950. "Pressure exchange apparatus". *US Patent 2,526,618*.

[13] Okamoto, K., and Nagashima, T., 2007. "Visualization of wave rotor inner flow dynamics". *J. Propul. Power,* ***23***(2), pp. 292–300.

[14] Araki, M., Ishima, T., Obokata, T., Arai, M., and Okamoto, K., 2007. "LDA measurement of an intermittent high-speed flow inside a micro wave rotor cell". *Proceedings of 2007 Fuels and Emissions Conference*(2), pp. 01–0010.

[15] Wijeyakulasuriya, S., Elharis, T., and Nalim, M., 2012. "Fuel proximity effect on hot-jet ignition in a wave rotor constant volume combustor". *AIAA Paper 2012-4171*.

[16] Li, J., Gong, E., Li, W., and Yuan, L., 2017. "Investigation on combustion properties in simplified wave rotor constant volume combustor". *AIAA paper 2017-2384*.

[17] Glick, H. S., 1958. "Shock tube studies of reaction kinetics of aliphatic hydrocarbons". *Symp. (Int.) Combust.,* ***7***(1), pp. 98–107.

[18] Glick, H. S., Squire, W., and Hertzberg, A., 1955. "A new shock tube technique for the study of high temperature gas phase reactions". *Symp. (Int.) Combust.,* ***5***(1), pp. 393–402.

[19] Rose, P. H., 1979. "Potential applications of wave machinery to energy and chemical processes". *Proceedings of the 12th International Symposium on Shock Tubes and Waves*, pp. 3–30.

[20] Wilson, J., Welch, G., and Paxson, D., 2007. "Experimental results of performance tests on a four-port wave rotor". *45th AIAA Aerospace Sciences Meeting and Exhibit*, p. 1250.

[21] Brouillette, M., 2003. "Shock waves at microscales". *Shock waves,* ***13***(1), pp. 3–12.

[22] Iancu, F., and Müller, N., 2006. "Efficiency of shock wave compression in a microchannel". *Microfluid. Nanofluid.,* ***2***(1), pp. 50–63.

[23] Welch, G. E., Jones, S. M., and Paxson, D. E., 1997. "Wave-rotor-enhanced gas turbine engines". *ASME J. Eng. Gas Turbines Power,* ***119***(2), pp. 469–477.

[24] Kurec, K., Piechna, J., and Gumowski, K., 2017. "Investigations on unsteady flow within a stationary passage of a pressure wave exchanger, by means of PIV measurements and CFD calculations". *Appl. Therm. Eng.,* ***112***(1), pp. 610–620.

[25] Hu, D., Li, R., Liu, P., and Zhao, J., 2016. "The design and influence of port arrangement on an improved wave rotor refrigerator performance". *Appl. Therm. Eng.,* ***107***(1), pp. 207–217.

[26] Tüchler, S., and Copeland, C. D., 2019. "Experimental results from the bath μ-wave rotor turbine performance tests". *Energy Convers. Manage.,* ***189***(1), pp. 33–48.

[27] Tüchler, S., and Copeland, C. D., 2020. "Experimental and numerical assessment of an optimised, non-axial wave rotor turbine". *Appl. Energy,* ***268***(1), p. 115013.

[28] Wullenkord, M., 2012. "Determination of kinetic parameters of the thermal dissociation of methane". *PhD Thesis*.

[29] Hu, D., Li, R., Liu, P., and Zhao, J., 2016. "The loss in charge process and effects on performance of wave rotor refrigerator". *Int. J. Heat Mass Transfer,* ***100***, pp. 497–507.